

Fourth RIT binary black hole simulations catalog: Extension to eccentric orbits

James Healy and Carlos O. Lousto[✉]

*Center for Computational Relativity and Gravitation, School of Mathematical Sciences,
Rochester Institute of Technology, 85 Lomb Memorial Drive, Rochester, New York 14623, USA*



(Received 31 January 2022; accepted 26 May 2022; published 7 June 2022)

This fourth release of the RIT public catalog of numerical relativity black-hole-binary waveforms consists of 1881 accurate simulations that include 446 precessing and 611 nonprecessing quasicircular/inspiraling binary systems with mass ratios $q = m_1/m_2$ in the range $1/128 \leq q \leq 1$ and individual spins up to $s/m^2 = 0.95$; and 824 in eccentric orbits in the range $0 < e \leq 1$. The catalog also provides initial parameters of the binary, trajectory information, peak radiation, and final remnant black hole properties. The waveforms are corrected for the center of mass drifting and are extrapolated to future null infinity. As an application of this waveform catalog we reanalyze all of the peak radiation and remnant properties to find new, simple, correlations among them, valid in the presence of eccentricity, for practical astrophysical usage.

DOI: 10.1103/PhysRevD.105.124010

I. INTRODUCTION

Since the breakthroughs [1–3] in numerical relativity solved the binary black hole problem those techniques have been used to explore the dynamics of spinning black-hole binaries beyond the post-Newtonian regime. The first generic, long-term precessing black-hole binary evolutions (i.e., without any symmetry) were performed in Ref. [4], where a detailed comparison with post-Newtonian $\ell = 2, 3$ waveforms modes was made. Numerical simulations have then explored the corners of parameter space, including near extremal spins $\chi = S_i/m_i^2 = 0.99$, binaries [5,6], mass ratios as small as $q = m_1/m_2 = 1/128$ in Ref. [7], and large initial separations, $R = 100m$, in Ref. [8]. Numerical relativity has also proved to be able to produce very long waveforms starting at proper separations of $25m$ for a precessing binary in [9] and for a nonspinning binary with 176 orbits to merger in Ref. [10].

Other important studies include the exploration of the *hangup* effect, i.e., the role individual black-hole spins play to delay or accelerate their merger [11–14], the determination of the magnitude and direction of the *recoil* velocity of the final merged black hole [15–22], and the *flip-flop* of individual spins during the orbital phase [9,23,24], the *L-flip* of the orbital angular momentum leading to beaconing of gravitational waves [25], as well as generic precession dynamics [26–29] and the inclusion of those dynamical effects to construct surrogate models for gravitational waveforms [30–32].

Numerical relativity predictions of the gravitational waveforms from the late inspiral, plunge, merger, and ringdown of black-hole-binary systems (BHB) based on

the breakthroughs [1–3] helped to accurately identify the first direct detection [33] of gravitational waves with that of binary black hole systems [34–37] and match them to targeted supercomputer simulations [38–41]. There have been several significant efforts to collect numerical relativity simulations into waveform catalogs released by the SXS collaboration [42–45], Georgia Tech. [46], and RIT [47–49]. The third RIT catalog release [49] reaching 777 simulations, was recently used for parameter estimation of all BBH O1/O2 gravitational waves signals from LIGO-Virgo in [50] and to assess theoretical definitions of the center of mass evolution of BBH systems in [51], among several other applications.

In this paper we describe a new release of the public waveform catalog by the RIT numerical relativity group that total 1881 simulations by adding a new set of 824 eccentric orbits waveforms, and 134 nonprecessing and 146 precessing quasicircular inspiraling binaries. The catalog includes all waveform modes $\ell \leq 4$ modes of the Weyl scalar ψ_4 and the strain H (both extrapolated to null-infinity) and is updated to correct for the center of mass displacement during inspiral and after merger. The catalog can be accessed from the site [52].

This paper is organized as follows. In Sec. II we briefly summarize the methods and criteria for producing the numerical simulations. In Sec. III we describe the relevant BHB parameters, the file format, and the content of the data in the catalog. In Sec. IV we describe the production of 824 eccentric simulations. In Sec. V we seek simple correlations among the black hole merger remnant and peak waveform parameters. Section VI concludes with a discussion of the future use of this catalog for parameter inference of new

gravitational waves events and the extensions of this work to longer, more generic precessing binaries.

II. FULL NUMERICAL EVOLUTIONS

The simulations in the RIT Catalog were evolved using the LazEv code [53] implementation of the moving puncture approach [2]. In most cases we use the BSSNOK formalism of evolutions systems [54–56]. (except for the very highly spinning holes, $\chi > 0.9$ where we use CCZ4 [57]). For the runs in the catalog, metadata, such as finite-difference orders, Kreiss-Oliger dissipation orders, and Courant factors [58–60] are included as references associated with each run (where detailed studies have been performed).

The LazEv code uses the CACTUS [61]/CARPET [62]/EinsteinToolkit [63,64] infrastructure. The CARPET mesh refinement driver provides a “moving boxes” style of mesh refinement. We use AHFinderDirect [65] to locate apparent horizons. We first measure the magnitude of the horizon spin S_H , using the *isolated horizon* algorithm as implemented in Ref. [66]. We can then calculate the horizon mass via the Christodoulou formula $m_H = \sqrt{m_{\text{irr}}^2 + S_H^2}/(4m_{\text{irr}}^2)$, where $m_{\text{irr}} = \sqrt{A_H/(16\pi)}$ and A_H is the surface area of the horizon.

To compute the numerical (Bowen-York) initial data, we use the TwoPunctures [67] code. To determine quasi-circular orbits we use the third post-Newtonian order techniques described in [68]. To produce eccentric orbital parameters, we reduce the tangential quasicircular linear momentum by a factor $(1 - \epsilon)$. We evaluate eccentricity during evolution via the simple formula, as a function of the separation of the holes, d , $e_d = d^2 \ddot{d}/m$, as given in [4].

In Ref. [69] to generate more realistic initial data with reduced spurious gravitational wave content, we have chosen a background ansatz of conformal superposition of (boosted) Kerr spatial metrics. These new initial data, denoted as HiSpID, are relevant for nonspinning as well as very highly spinning black holes in a binary [6], and high energy collisions [70]. To generate those data we generalized the TwoPunctures code [67] to solve a coupled system of the Hamiltonian and momentum constraints. We use these data for evolving highly spinning binaries with intrinsic spins $\chi_i = S_i/m_i^2 > 0.9$.

We measure radiated energy, linear momentum, and angular momentum, in terms of the radiative Weyl scalar ψ_4 , using the formulas provided in Refs. [71,72]. As described in Ref. [73], we use the Teukolsky equation to analytically extrapolate expressions for $r\psi_4$ to \mathcal{I}^+

In Ref. [49] we describe a practical implementation of the center of mass correction to account for a linear shift in time of the origin of coordinates for the multipole decomposition of the waveform (See Ref. [74]). This shift can be performed *a posteriori*, by demixing modes at each time step from a center of coordinates that is linearly moving [75].

Several cases presented in this catalog have been studied in detail to evaluate typical errors. In Appendix A of Ref. [76], in Appendix B of Ref. [60], and in Ref. [77], we performed convergence studies for different mass ratios and spins of the binaries. In Ref. [40] and Ref. [78] we compared the RIT waveforms with those produced completely independently by the SXS collaboration finding excellent agreement, convergence toward each others results and matching of individual modes up to $l = 5$.

We concluded that the waveforms at the resolutions provided in this catalog are well into the convergence regime (roughly converging at 4th-order with resolution), that the horizon evaluated quantities such as the remnant final mass and spins have typical errors of the order of 0.1%, and that the radiatively computed quantities such as the recoil velocities and peak luminosities are evaluated at a typical error of 5%.

A more detailed account of our full numerical techniques is described in Sec. II of Ref. [49] and references therein.

III. THE CATALOG

The RIT Catalog can be found at [52]. Figure 1 shows the distribution of the nonprecessing runs in the catalog in terms of $\chi_{1,2}$ and q (where χ_i^ζ is the component of the dimensionless spins of BH i along the direction of the orbital angular momentum). The information currently in the catalog consists of the metadata describing the runs and all modes up through the $\ell = 4$ modes of $m\psi_4$ extrapolated to \mathcal{I}^+ via the perturbative approach of [73] (in this paper m represents the total mass of the system). The associated metadata include the initial orbital frequencies, ADM masses, initial waveform frequencies from (2,2) mode, black hole masses, momenta, spins, separations, and eccentricities, as well the black-hole masses and spins once the initial burst of radiation has left the region around the binary. *Relaxed* quantities (at $t_{\text{relax}} = 200m$ after the initial burst of radiation has mostly dissipated) are more accurate and physically relevant for modeling purposes. We normalize our data such that the sum of the two initial horizon masses is 1. In addition, we also include peak luminosities, amplitude, and frequency, and the final remnant black hole masses, spins, and recoil velocities.

The catalog is organized using an interactive table [79] that includes an identification number, resolution, type of run (nonspinning, aligned spins, precessing), the initial proper length of the coordinate line joining the two BH centroids between the two horizons [8], the coordinate separation of the two centroids, the mass ratio of the two black holes, the components of the dimensionless spins of the two black holes, the starting waveform frequency, $m f_{22,\text{relax}}$, time to merger, number of gravitational wave cycles calculated from the (2,2) modes from the beginning of the inspiral signal to the amplitude peak, remnant mass, remnant spin, recoil velocity, and peak luminosity. The final column gives bibtex keys for the relevant publications

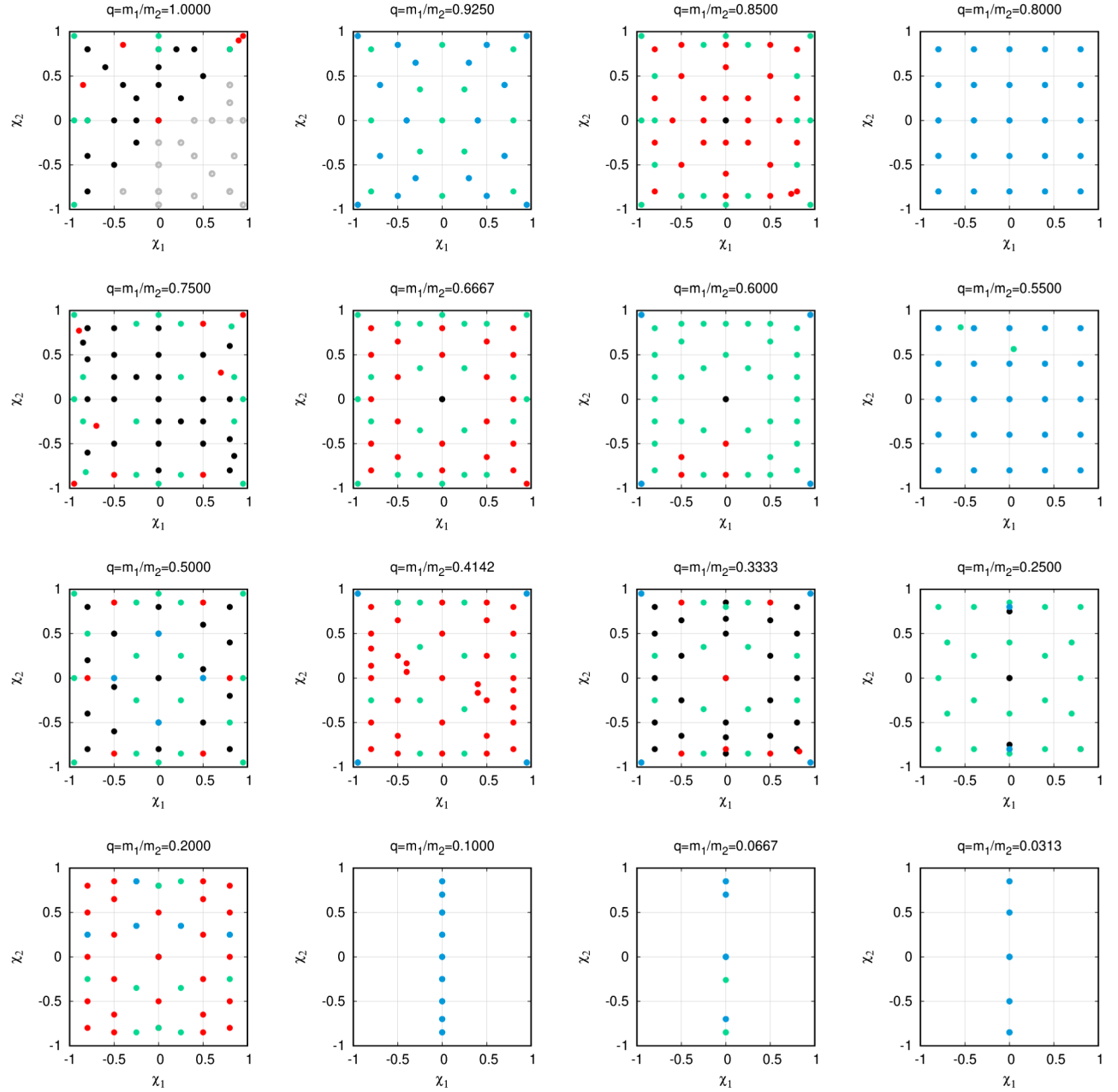


FIG. 1. Initial parameters in the (q, χ_1^z, χ_2^z) space for the 611 quasicircular nonprecessing binaries. Note that χ_i denotes the component of the dimensionless spin of BH i along the orbital angular momentum $\hat{L} = \hat{z}$. Each panel corresponds to a given mass ratio that covers the comparable masses binary range from $q = 1$ to $q = 1/32$ (the nonspinning $q = 1/64, 1/128$ not shown here). The dots in black denote the simulations of the catalog first release, the dots in red are those of the second release, the dots in green are those of this third release, and the dots in blue are those of this fourth release.

where the waveforms were first presented. The table can be sorted (ascending or descending) by any of these columns, and there is a direct search feature that runs over all table elements. Resolutions are given in terms of the grid spacing of the refinement level where the waveform is extracted (which is typically two refinement levels below the coarsest grid, where external boundaries of the simulation lies) with the observer location typically about $R_{\text{obs}} \sim 100m$. We use the notation nXYY, where the grid spacing in the

wavezone is given by $h = m/X.YY$, e.g., n120 corresponds to $h = m/1.2$, n140 corresponds to $h = m/1.4$, and so on. We specify the resolution used in each simulation, typically corresponding to a medium resolution, as found from a few representative cases studied at multiple resolutions around n100. For the eccentric simulations described below in Sec. IV see the Supplementary Material in the paper [80].

For each simulation in the catalog there are three files: one contains the metadata information in ASCII format, the

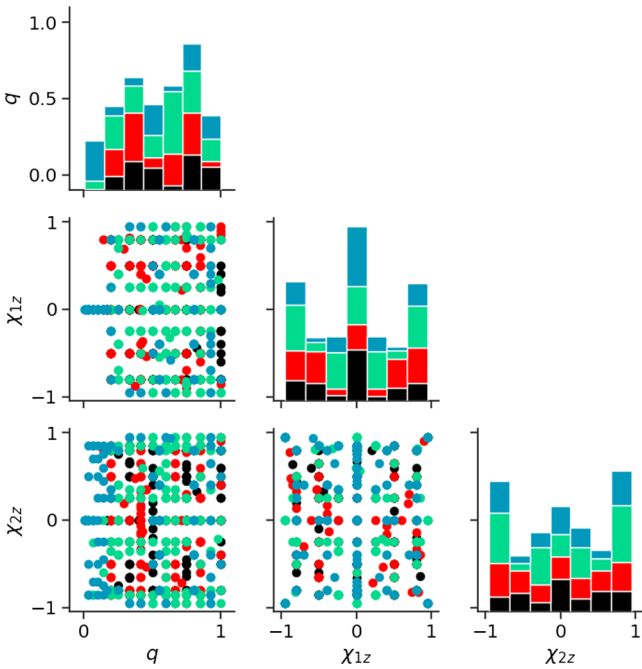


FIG. 2. Counting simulations in the (q, χ_1^z, χ_2^z) planes (faces of the cube) for the 611 nonprecessing binaries. The 120 release 1 simulations are black, the 154 release 2 simulations are red, the 203 release 3 are in green, and the 134 release 4 are in blue.

other two are a tar.gz files containing ASCII files with up to and including $\ell = 4$ modes of $m\psi_4$ and H . The primary data in our catalog is the Weyl scalar $m\psi_4$ extrapolated to \mathcal{I}^+ (using Eq. (29) of Ref. [73]), rather than the strain $(r/m)H$, that is also provided as a double time integration of $m\psi_4$.

Figure 2 shows a histogram of the distribution of the 611 nonprecessing runs in the catalog in terms of $\chi_{1,2}^z$ and q . Those runs were motivated by systematic studies to produce a set of accurate remnant formulas to represent the final mass, spin and recoil of a merged binary black hole system and the peak luminosity, amplitude and frequency, as a function of the parameters of the precursor binary, as reported in [14,49,60,76,81–83]. Another important motivation was to provide a grid of simulations for parameter estimation of gravitational wave signals detected by LIGO-Virgo using the methods described in [38,50].

The precessing quasicircular runs in the catalog were motivated to study particular spin dynamics of merging BHB, such as the study of unstable spin flip-flop [24], beacons (L-flip) [25], and targeted followups of gravitational wave signal from the first and second LIGO-Virgo observing runs [40,50,78]. We have supplemented here the 300 precessing simulations of the third catalog release with additional 146 simulations that improve the coverage of spin orientations (see Fig. 8).

Figure 3 shows the distributions of the minimal total mass of the 1047 quasicircular BHB systems in this fourth catalog release given a starting gravitational wave

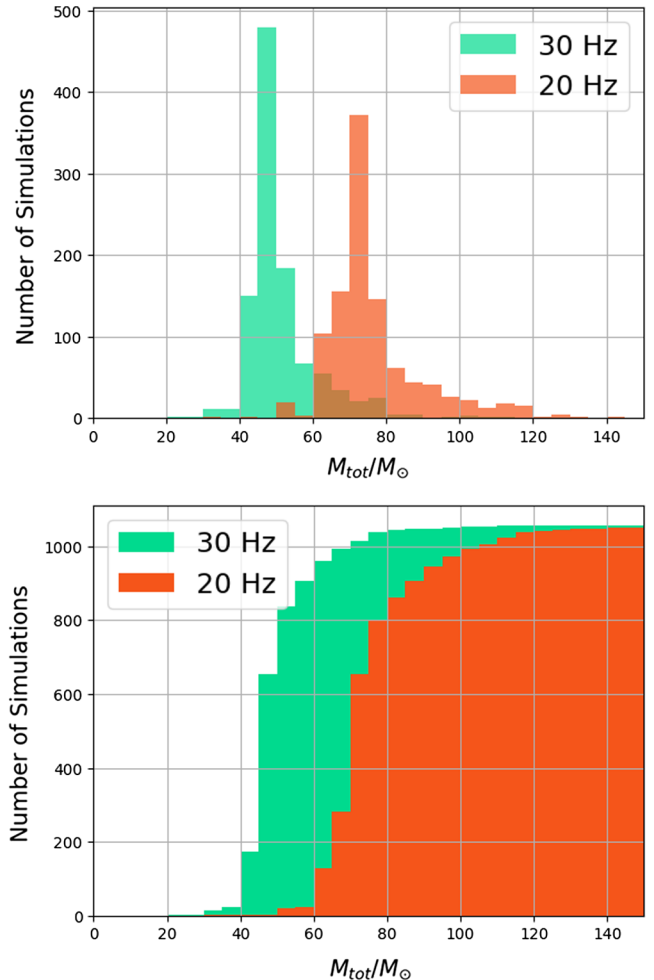


FIG. 3. Top: distributions of the total mass of BHB systems in the RIT catalog corresponding to a starting gravitational wave (2,2) mode frequency of 20 Hz (green) and 30 Hz (red) in bins of $5 M_\odot$. Bottom: the cumulative version of the above plot also in bins of $5 M_\odot$ for the 1057 quasicircular simulations in this catalog.

frequency of the (2,2) mode of 20 Hz or 30 Hz in the source frame (redshift effects improve this coverage in the detector frame by a factor of $1/(1+z)$ in frequency, where z is the redshift).

IV. EXTENSION TO ECCENTRIC MERGING BINARIES

Three body encounters and accretion effects (see, e.g., [84–87]) can lead to highly eccentric binaries, with residual eccentricity surviving down to merger, and these eccentric binaries may have very interesting gravitational waves signals that cannot be adequately modeled using quasicircular approximations. This subject has been the focus of great interest lately [88–90], but its detailed modeling is largely incomplete. Reliable evolutions between LISA and LIGO bands can also be used to exploit multiband observational opportunities [91–93].

In Ref. [80] we show that GW190521 is most consistent with a highly eccentric black hole merger. We carried out 619 numerical relativity eccentric simulations to generate an effective $\sim 6 \times 10^4$ gravitational waveforms with different total masses to compare to the observed data. We found that GW190521 is best explained by a high-eccentricity, precessing model with $e \sim 0.7$ at the start of the simulation. All properties of GW190521 point to its origin being the repeated gravitational capture of black holes, making GW190521 the first of LIGO/Virgo's discovery whose formation channel is identified. We carried out eccentric binary black hole simulations in this study, with eccentricities in the full $e \in [0, 1]$ range. These simulations included nonspinning, aligned-spin and spin-precessing waveforms, and mass ratios $1/7 \leq q = m_2/m_1 \leq 1$. We first carried out a thorough survey of the eccentricity-mass ratio parameter space with nonspinning simulations. Then we carried out aligned/antialigned spin and precessing simulations for a broad range of eccentricity values, most densely covering the parts of the parameter space where the non-spinning simulations produced the highest likelihood $\log \mathcal{L}_{\text{marg}}$ in comparison to GW190521 signal. For precessing waveforms we most densely targeted the $\chi_p \sim 0.7$ case expected from black hole merger remnants. Our simulated gravitational waveforms were then scaled to correspond to different black hole masses, providing about 100 scaled mass values for each simulation in order to best match the total mass of the GW190521 event.

As a control that our eccentric simulations are in the convergence regime we display in Table I a three numerical resolutions study of the remnant black hole parameters from two of the top matching waveforms to the GW190521 event. To find a convergence rate n for a given resolution h we have match the dependence of the remnant quantities of the final mass, spin, and recoil, m_f , α_f , V_f to the generic form $A + Bh^n$, where A is the extrapolation to infinite resolution n_∞ and B a fitting

TABLE I. Convergence of the remnant final mass, spin, and recoil, m_f , α_f , V_f for two representative eccentric simulations.

Catalog no.	Resolution	m_f	α_f	V_f [km/s]
RIT: eBBH:1637	n100	0.9584505	0.7830475	0.0000190
	n120	0.9580466	0.7822618	0.0000057
	n144	0.9578167	0.7818401	0.0000044
	rate	3.1	3.4	12
	n_∞	0.9575130	0.7813514	0.0000043
	$*n_\infty$	0.9575095	0.7813336	0.0000169
RIT: eBBH:1707	n100	0.9628020	0.7507813	2038.728
	n120	0.9625190	0.7501863	2060.747
	n144	0.9623622	0.7498763	2072.700
	rate	3.24	3.56	3.35
	n_∞	0.9621676	0.7495390	2086.892
	$*n_\infty$	0.9621624	0.7495262	2087.372

constant. We also provide the alternative extrapolation to infinite resolution $*n_\infty$ by matching to $A + Bh^3 + Ch^4$ to show the robustness of the results with the expected convergence rate dominated by the 4th order Runge-Kutta time integration used in our full numerical simulations (note that the recoil velocity of RIT:eBBH:1637 by symmetry should be zero). Note also that the extrapolated to infinite resolution values lie well within a fraction of a percent the standard resolution (n100) used in most of the catalog's simulations.

Here we report on 632 runs with a reference quasicircular gravitational wave (2,2) mode frequency of 10 Hz for a total system mass of $50 M_\odot$ (motivated by the above mentioned target study for GW190521 [80]). It includes 115 precessing eccentric binaries and 517 nonprecessing of which 319 are nonspinning covering mass ratios from $q = 1/128$ to $q = 1$; and 198 have aligned (or counter-aligned) spins with the orbital angular momentum. In particular we include here the nonspinning binaries with mass ratios $q = 1/32, 1/64, 1/128$ studied in [94,95].

In addition we performed another set of eccentric binaries studies with a quasicircular gravitational wave (2,2) mode reference frequency of 30 Hz for a total system mass of $50 M_\odot$ corresponding to 192 nonspinning binaries bearing mass ratios $q = 1, 0.75, 0.50, 0.25$.

The numerical simulations techniques described in Sec. II also apply to accurately evolve eccentric binaries. To compute the numerical initial data, we use the puncture approach [96] along with the TwoPunctures [67] code. For each eccentric family, we first determine the initial separation and tangential quasicircular momentum that leads to a (2,2) mode frequency of 10 Hz for a $50 M_\odot$ system, using the post-Newtonian techniques described in [68]. To increase the eccentricity of the system while keeping the initial data at an apocenter, the initial tangential momentum is modified by parameter, $0 < \epsilon < 1$, such that $p_t = p_{t,qc}(1 - \epsilon)$. This provides a unique and invariant way of characterizing eccentric orbits at the start of the simulation. The corresponding initial orbital frequency (and (2,2)-modes of the gravitational waves) gets reduced by the same factor $\Omega_e = \Omega_{qc}(1 - \epsilon)$. The initial eccentricity is then approximately $e = 2\epsilon - \epsilon^2$, which contains the correct limits for $e = 0, 1$ at $\epsilon = 0, 1$. We plan to extend this definition to higher PN order to improve the identification of high eccentricities. Late time behavior of the eccentricity could be extracted, for instance, from the waveforms or proper distances at a post-processing level.

Figure 4 shows the distributions of the minimal total mass of the 824 eccentric BHB systems in this fourth catalog release given a starting gravitational wave frequency of the (2,2) mode of 20 Hz or 30 Hz in the source frame.

Figure 5 shows the distribution of the 611 quasicircular and 709 eccentric nonprecessing runs in the catalog,

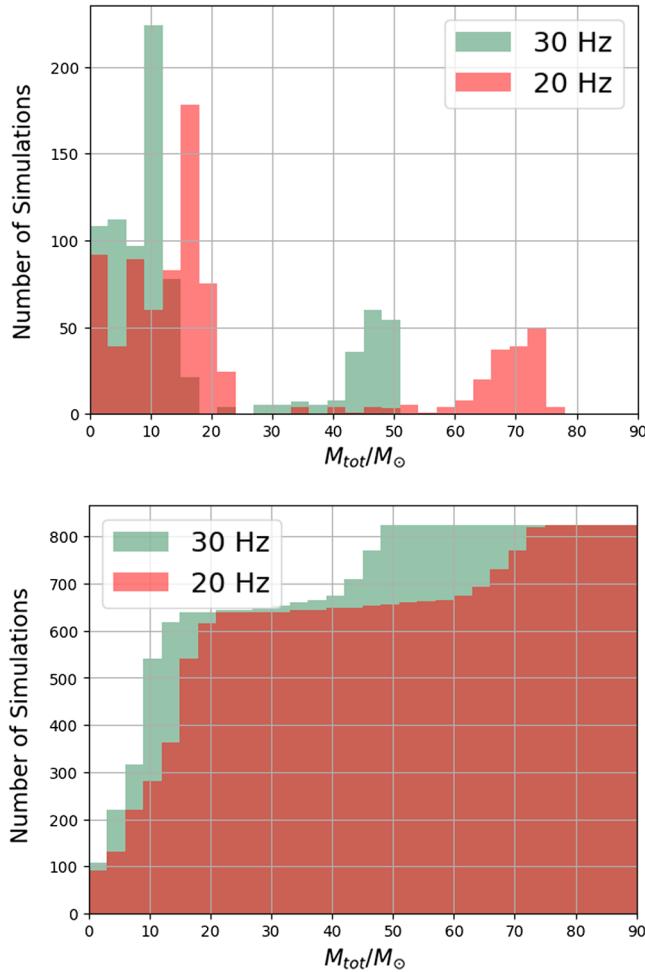


FIG. 4. Top: distributions of the total mass of BHB systems in the RIT catalog corresponding to a starting gravitational wave (2,2) mode frequency of 20 Hz (green) and 30 Hz (red) in bins of $3 M_{\odot}$. Bottom: the cumulative version of the above plot also in bins of $3 M_{\odot}$ for the 824 eccentric simulations in this catalog.

per release, in terms of the spins $\chi_{1,2}^z$, mass ratios q and eccentricity e .

V. MERGING BINARIES CORRELATIONS

Detailed and higher order formulas relating the binary parameters to the post-merger properties of the final remnant black hole and merger waveform have been studied in Refs. [14,60,76] using the aligned spins simulations of previous releases of the RIT catalog.

Foreseeing astrophysical applications of future massive catalogs of binary black holes, we display in Fig. 6 simple scaling phenomenological correlations between remnant parameters and merger waveforms for quasicircular binaries.

Fitting formulas of the form $f(x) = a + b \cdot \exp(c \cdot x)$ for these simple correlations and estimated errors of their fitted coefficient are given by

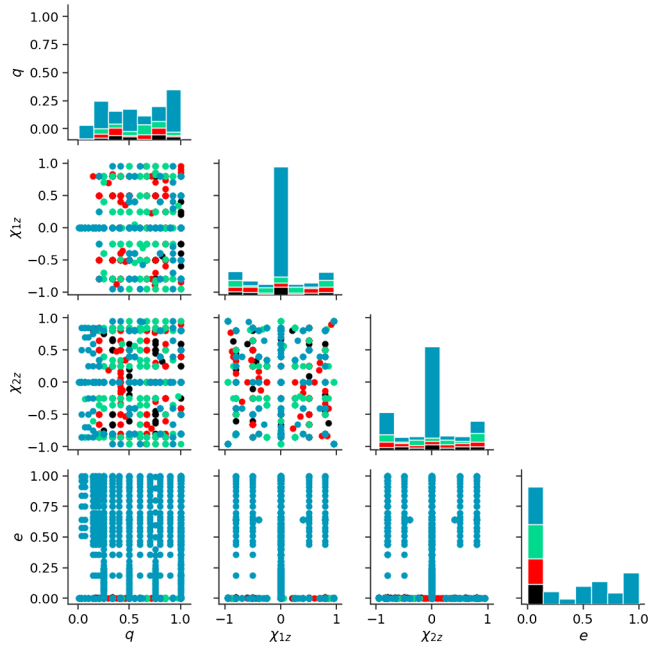


FIG. 5. Counting simulations in the $(q, \chi_1^z, \chi_2^z, e)$ planes (faces of the 4-cube) for the 1320 nonprecessing binaries. The 120 release 1 simulations are black, the 154 release 2 simulations are red, the 203 release 3 are in green, and the 843 release 4 in blue.

$$\begin{aligned}\alpha_f &= 1.049 \pm 0.007 - (27.07 \pm 0.97)e^{(-12.05 \pm 0.15)m\omega_{22}}, \\ \alpha_f &= 0.980 \pm 0.001 - (2.99 \pm 0.09)e^{(-288.85 \pm 7.96)\mathcal{L}/\eta^{1.5}}, \\ \alpha_f &= 0.971 \pm 0.009 - (2.48 \pm 0.04)e^{(-11.21 \pm 0.25)E_{\text{rad}}/\eta},\end{aligned}\quad (1)$$

for the final spin α_f as a function of the peak frequency $m\omega_{22}$ of the (2,2) mode, the peak luminosity \mathcal{L} , and the total radiated energy during merger E_{rad} (normalized by the symmetric mass ratio $\eta = q/(1+q)$). The typical error in the fitted coefficients amount to less than 3%. Note that the application of the fits should be for intermediate mass ratios. In particular the spin versus small E_{rad} and \mathcal{L} will be dominated in the small mass ratio regime by the (original) spin of the large hole and hence the observed branching off of curves at those small values.

Similar correlations among other quantities are,

$$\begin{aligned}\mathcal{L}/\eta^{1.5} &= 0.027 \pm 0.001 - (0.027 \pm 0.001)e^{(-2.05 \pm 0.10)E_{\text{rad}}/\eta}, \\ \mathcal{L}/\eta^{1.5} &= 0.138 \pm 0.136 - (0.151 \pm 0.135)e^{(-0.40 \pm 0.42)m\omega_{22}}, \\ m\omega_{22} &= 0.562 \pm 0.013 - (0.38 \pm 0.01)e^{(-3.32 \pm 0.21)E_{\text{rad}}/\eta}, \\ m\omega_{22} &= 1.487 \pm 0.048 - (1.28 \pm 0.48)e^{(-15.24 \pm 6.50)\mathcal{L}/\eta^{1.5}}\end{aligned}\quad (2)$$

In the case of the eccentric binaries we will seek for similar correlations that also involve only the nonprecessing simulations for which we have a set of 709 simulations, all in this fourth catalog release that we display in Fig. 7.

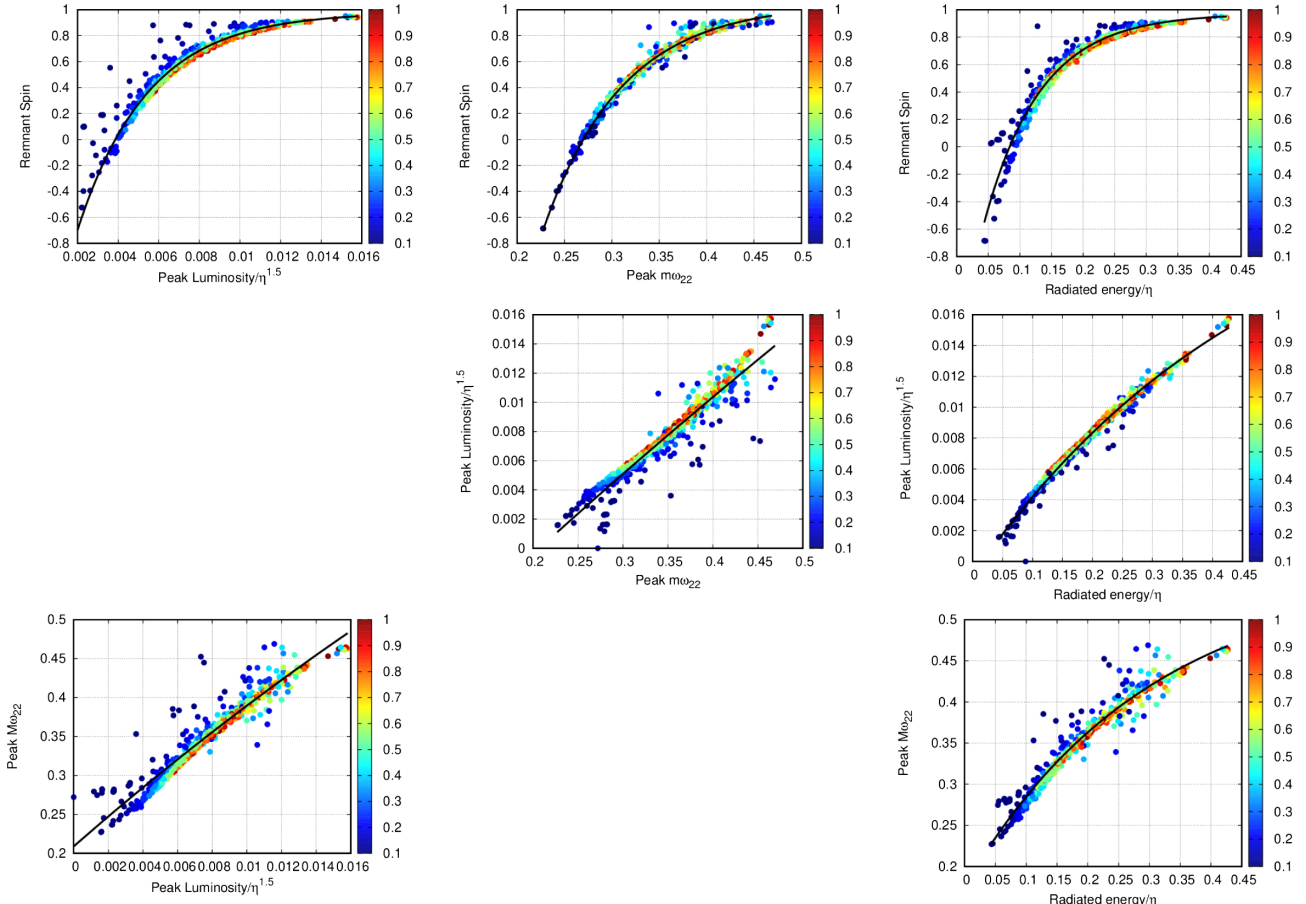


FIG. 6. Correlations between the radiated energy, peak luminosity, peak frequency at merger and spin remnant with the corresponding leading scaling by the symmetric mass ratio. Color column bar corresponds to different mass ratios of these quasicircular simulations.

Fitting formulas for the simple correlations and estimated errors in their coefficient are

$$\begin{aligned} \mathcal{L}/\eta^{1.5} &= (0.00033 \pm 0.000026)e^{(8.87 \pm 0.22)m\omega_{22}}, \\ \mathcal{L}/\eta^{1.5} &= (0.00019 \pm 0.000016)e^{(2.30 \pm 0.05)(r/m)H_{22}/\eta}, \\ \mathcal{L}/\eta^{1.5} &= (0.0162 \pm 0.001) - (0.018 \pm 0.0008) \\ &\quad \times e^{(-4.58 \pm 0.47)E_{\text{rad}}/\eta}, \end{aligned} \quad (3)$$

for the final peak luminosity \mathcal{L} as a function of the peak frequency $m\omega_{22}$ and waveform amplitude H_{22} (extrapolated to \mathcal{I}^+) of the (2,2) mode, and the total radiated energy during merger E_{rad} [normalized by the symmetric mass ratio $\eta = q/(1+q)$].

Other correlations among those quantities can be found,

$$\begin{aligned} m\omega_{22} &= (0.141 \pm 0.003)e^{(0.558 \pm 0.016)\frac{r}{m}H_{22}/\eta}, \\ m\omega_{22} &= (0.357 \pm 0.003) - (0.385 \pm 0.0027) \\ &\quad \times e^{(-22.69 \pm 1.70)E_{\text{rad}}/\eta}, \\ (r/m)H_{22}/\eta &= (1.635 \pm 0.011) - (2.29 \pm 0.14) \\ &\quad \times e^{(-24.52 \pm 1.41)E_{\text{rad}}/\eta}. \end{aligned} \quad (4)$$

These correlations for highly eccentric orbits carry larger errors than the corresponding correlations for quasicircular/inspiral orbits, but still could be used in astrophysical estimates. Their range of validity should be for intermediate mass ratios and in their positive values, where these simple formulas have been fitted and we have not tested them in the extrapolation regime.

VI. CONCLUSIONS AND DISCUSSION

The 2005 numerical relativity breakthroughs [1–3] were instrumental in identifying the first detection of gravitational waves [33] with the merger of two black holes. Those different approaches to solve the binary black hole problem produced an excellent agreement for the modeling of the sources of GW150914 [40] and GW170104 [78], including comparison of higher (up to $\ell = 5$) modes. The recent success of applying eccentric orbits simulations to describe the source of GW190521 [80] highlights the importance of the direct use of numerical relativity waveforms to model sources of gravitational waves events.

In particular, we used the third RIT Catalog release [49] to reanalyze the ten binary black hole events reported by the

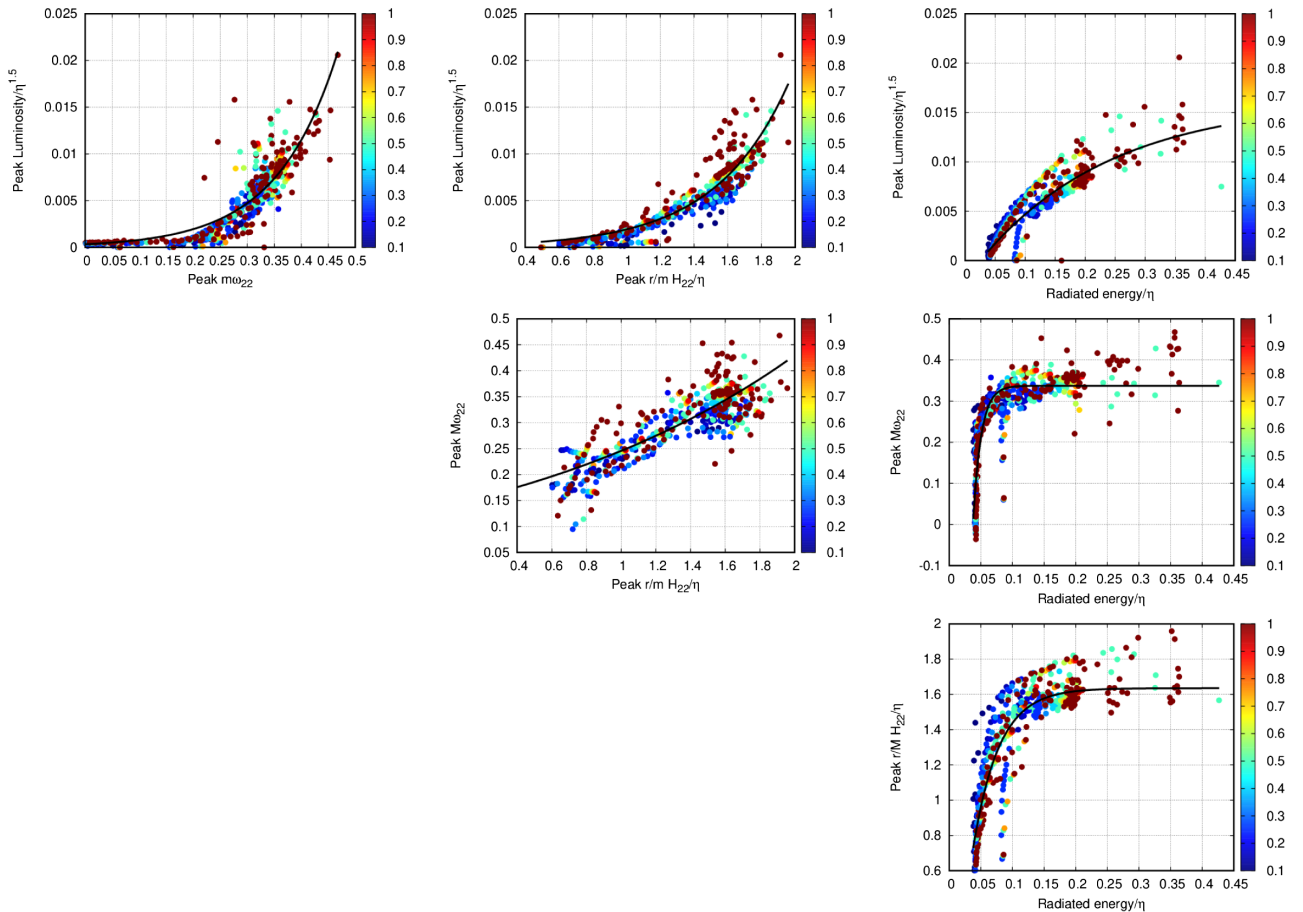


FIG. 7. Phenomenological correlations for eccentric binaries between the radiated energy, peak luminosity, peak frequency at merger with the corresponding scaling by the symmetric mass ratio η to obtain the leading dependences. The color column bar on the right corresponds to different mass ratios.

LIGO-Virgo collaboration for the O1/O2 observational runs [97], confirming, and sometimes improving their parameter estimations [50]. We have also succeeded in confirming the parameters of three additional black hole binary merger events, displaying again the importance of the use of numerical relativity waveform catalogs as a consistent method for parameter estimation.

TABLE II. Summary of simulations in each release of the RIT catalog.

Release/[cite]	No. 1 [47]	No. 2 [48]	No. 3 [49]	No. 4 (In this paper)	
				Total	No. 4
QC nonspinning	21	4	4	14	43
QC aligned	99	150	199	120	568
QC precessing	6	40	254	146	446
Eccentric nonspinning	511	511
Eccentric aligned	198	198
Eccentric precessing	115	115
Subtotal	126	194	457	1104	1881

The next areas of development for the numerical relativity waveform catalogs include the coverage of precessing binaries. Those require expansion of the parameter space to eight dimensions (including now eccentricity), and can be carried out in a hierarchical approach by first neglecting the effects of the spin of the secondary black hole, which is a good assumption for small mass ratios. Other lines of extension of the catalogs include very highly spinning black holes with spin magnitudes in the range $\chi = 0.95\text{--}0.99$. And smaller mass ratio binaries to complete the family of simulations displayed in Fig. 1, i.e., $q = 1/10, 1/15, 1/32$ and include spins of the large hole in the $q = 1/64, 1/128$ simulations. These small mass ratio simulations, in turn, can inform the modeling through phenomenological approaches, like the use of effective one body (EOB) models. While low (below $20 M_\odot$) total binary masses, require longer full numerical simulations or hybridization of the current numerical relativity waveforms with post-Newtonian waveforms [98].

Simulations of black-hole binaries also produce information about the final remnant of the merger. Several empirical formulas relating the initial parameters ($q, \vec{\chi}_1, \vec{\chi}_2$)

(individual masses and spins) of the binary to those of the final remnant ($m_f, \vec{\alpha}_f, \vec{V}_f$) have been proposed for the final mass, spin, and recoil velocity [13,76,83,99–106], the computation of the peak frequency of the (2,2) mode $\Omega_{22}^{\text{peak}}$, peak waveform amplitude H_{22}^{peak} [14,77] and peak luminosity [33,36,60,81]. The tables in the Appendix can be used to further model those remnant formulas and to include eccentricity as an additional parameter and to test remnant and merger waveform parameters in terms

of those of the inspiraling binary as a consistency test for the theory of gravity.

We finally summarize here the number of simulations per release in Table II with a distinction of quasicircular (QC) and eccentric orbits and by discriminating binary black holes on being both nonspinning or spinning but nonprecessing, and full precessing.

A visual representation of the 446 binaries' in the 7 QC parameter precessing space is displayed in Fig. 8. Here $\chi_{i\parallel}$

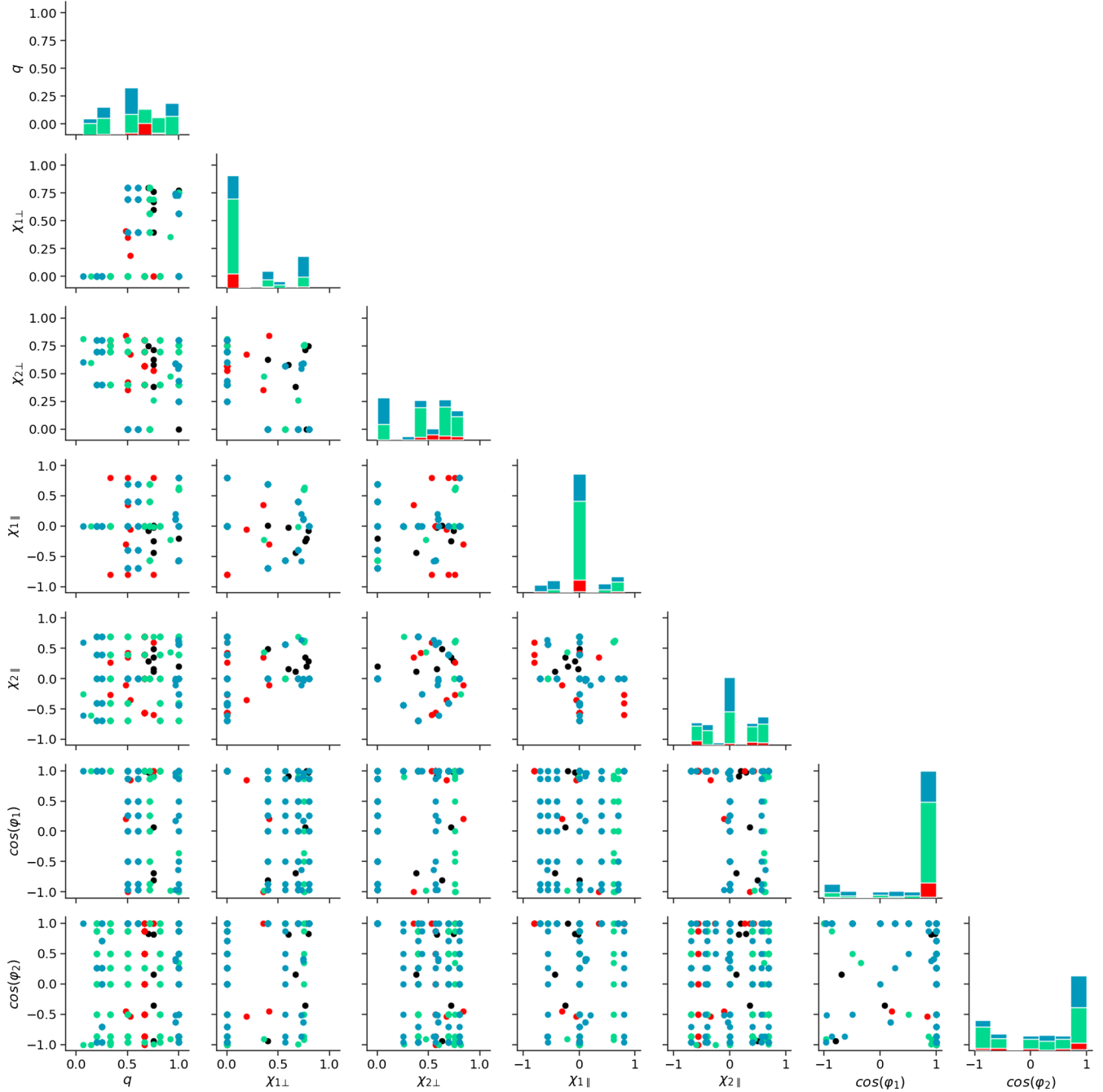


FIG. 8. Panels showing different combinations of the 7 binary parameters of the precessing parameter space ($q, \chi_{1\parallel}, \chi_{1\perp}, \varphi_1, \chi_{2\parallel}, \chi_{2\perp}, \varphi_2$) for the 446 quasicircular simulations (black first release, red second release, green third release, blue fourth release) in this catalog.

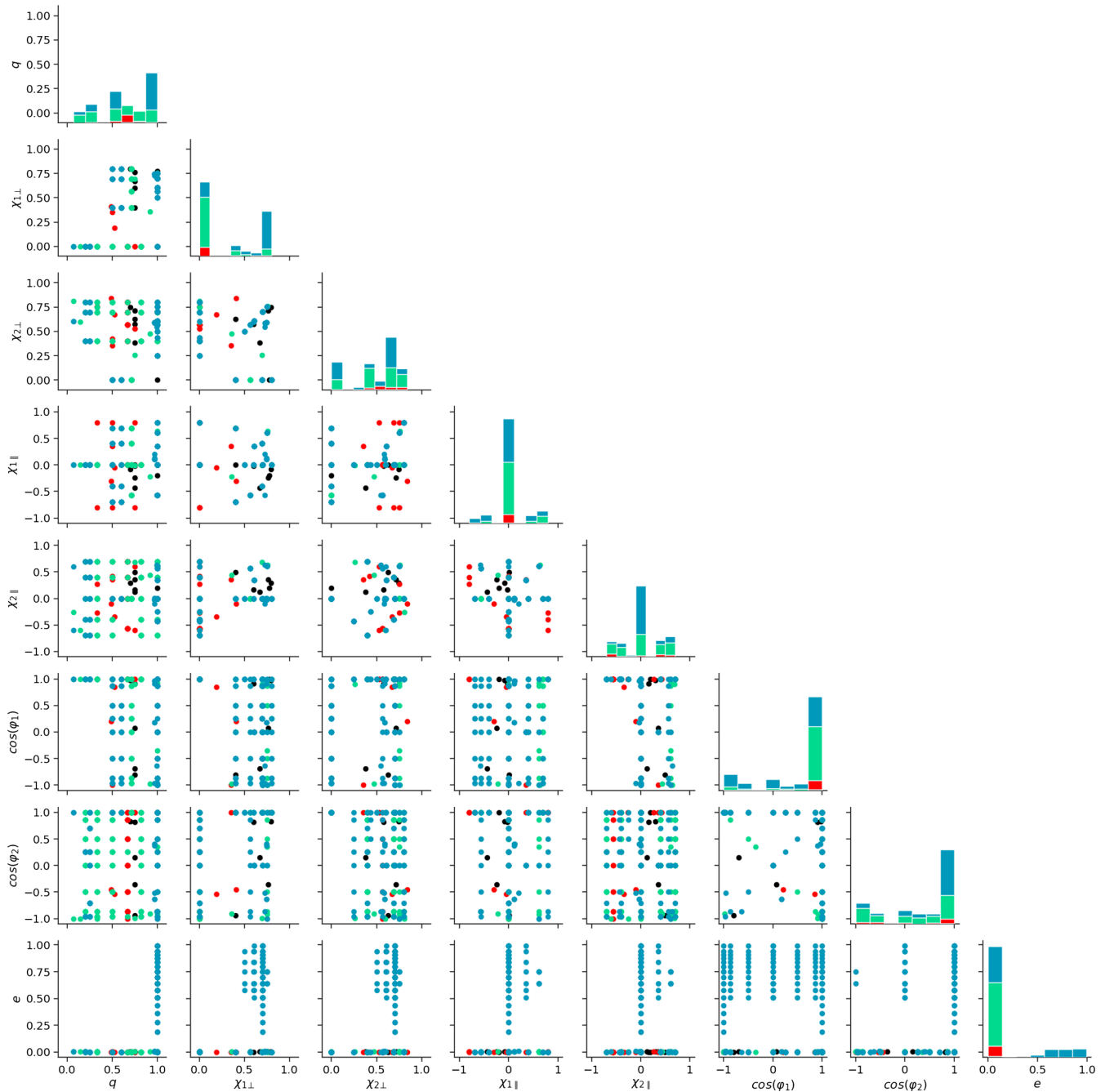


FIG. 9. Panels showing different combinations of the 8 binary parameters of the precessing parameter space ($q, \varphi_2 \chi_{1\parallel}, \chi_{1\perp}, \varphi_1, \chi_{2\parallel}, \chi_{2\perp}, \varphi_2, e$) for the 561 eccentric simulations (black first release, red second release, green third release, blue fourth release) in this catalog.

refers to the projection of the spins along the orbital angular momentum direction \hat{L} and $\chi_{i\perp}$ the perpendicular to it.

While a visualization of the 561 highly eccentric binaries' in the 8 parameter precessing space is displayed in Fig. 9.

ACKNOWLEDGMENTS

The authors gratefully acknowledge the National Science Foundation (NSF) for financial support from

Grant No. PHY-1912632. Computational resources were also provided by the NewHorizons, BlueSky Clusters, Green Prairies, and White Lagoon at the Rochester Institute of Technology, which were supported by NSF Grants No. PHY-0722703, No. DMS-0820923, No. AST-1028087, No. PHY-1229173, No. PHY-1726215, and No. PHY-2018420. This work used the Extreme Science and Engineering Discovery Environment (XSEDE) [allocation TG-PHY060027N], which is supported by NSF

TABLE VI. The mass and spin of the 146 QC precessing BHs in Table III after the BHs had time to equilibrate ($t/m = 200$).

Run	q^r	m_1^r/m	m_2^r/m	χ_{1x}^r	χ_{1y}^r	χ_{1z}^r	χ_{2x}^r	χ_{2y}^r	χ_{2z}^r
RIT:BBH:0787	0.5998	0.3749	0.6250	-0.3116	0.2257	0.7021
RIT:BBH:0791	0.0667	0.0625	0.9367	0.6030	0.0334	-0.6002
RIT:BBH:0806	0.4998	0.3332	0.6667	0.3450	0.2137	-0.6904
RIT:BBH:0807	0.2001	0.1667	0.8329	-0.3775	-0.1337	-0.6937
RIT:BBH:0808	0.2001	0.1667	0.8329	0.1346	-0.3819	-0.6911
RIT:BBH:0811	0.5998	0.3749	0.6250	-0.3115	-0.2618	0.6895
RIT:BBH:0813	0.2001	0.1667	0.8329	-0.6522	-0.2397	-0.3984
RIT:BBH:0814	0.5998	0.3749	0.6250	-0.3874	0.0232	0.7002
RIT:BBH:0815	0.2001	0.1667	0.8329	0.2396	-0.6528	-0.3974
RIT:BBH:0816	0.2001	0.1667	0.8329	-0.7550	-0.2673	0.0006
RIT:BBH:0817	0.2001	0.1667	0.8329	0.2668	-0.7552	0.0061
RIT:BBH:0818	0.5998	0.3749	0.6250	0.6148	0.3212	0.3999
RIT:BBH:0821	0.5998	0.3749	0.6250	0.0916	0.6883	0.3983
RIT:BBH:0822	0.5998	0.3749	0.6250	0.2369	-0.3220	0.6936
RIT:BBH:0823	0.2001	0.1667	0.8329	-0.6501	-0.2392	0.4021
RIT:BBH:0824	0.2001	0.1667	0.8329	0.2100	-0.6628	0.3976
RIT:BBH:0826	0.2001	0.1667	0.8329	-0.3765	-0.1334	0.6943
RIT:BBH:0827	0.5998	0.3749	0.6250	0.4005	0.5727	0.3905
RIT:BBH:0828	0.2001	0.1667	0.8329	0.1037	-0.3868	0.6937
RIT:BBH:0832	0.5998	0.3749	0.6250	0.3439	0.2097	-0.6920
RIT:BBH:0834	0.5999	0.3749	0.6250	-0.2518	0.6320	0.4217
RIT:BBH:0835	0.4999	0.3332	0.6667	0.0095	0.4159	-0.6842
RIT:BBH:0839	0.4998	0.3332	0.6667	0.2087	0.3614	-0.6835
RIT:BBH:0842	0.5999	0.3749	0.6250	-0.5545	0.3919	0.4239
RIT:BBH:0845	0.4999	0.3332	0.6667	-0.3357	0.2306	-0.6895
RIT:BBH:0846	0.5998	0.3749	0.6250	-0.6819	0.0350	0.4180
RIT:BBH:0847	0.5998	0.3749	0.6250	0.2083	0.3582	-0.6851
RIT:BBH:0848	0.4999	0.3332	0.6667	-0.1668	0.3520	-0.6997
RIT:BBH:0849	0.5998	0.3749	0.6250	-0.1768	0.3628	-0.6914
RIT:BBH:0850	0.4998	0.3332	0.6667	0.6838	0.4164	0.0091
RIT:BBH:0851	0.4998	0.3332	0.6667	-0.4071	0.0098	-0.6896
RIT:BBH:0852	0.5998	0.3749	0.6250	0.0156	0.4145	-0.6848
RIT:BBH:0853	0.4999	0.3333	0.6667	-0.3192	0.7337	0.0168
RIT:BBH:0854	0.4999	0.3332	0.6667	0.4143	0.6852	0.0057
RIT:BBH:0855	0.4999	0.3333	0.6667	0.0771	0.7968	0.0059
RIT:BBH:0856	0.4999	0.3332	0.6667	-0.8004	0.0136	0.0158
RIT:BBH:0857	0.4999	0.3333	0.6667	-0.6700	0.4378	0.0185
RIT:BBH:0858	0.4998	0.3332	0.6667	0.3470	0.6118	-0.3827
RIT:BBH:0859	0.5998	0.3749	0.6250	-0.3338	0.2330	-0.6894
RIT:BBH:0860	0.4999	0.3333	0.6667	0.0573	0.6974	-0.3890
RIT:BBH:0861	0.4999	0.3333	0.6667	-0.2831	0.6359	-0.3954
RIT:BBH:0862	0.4999	0.3333	0.6667	-0.5845	0.3787	-0.3948
RIT:BBH:0863	0.5998	0.3749	0.6250	-0.4066	0.0151	-0.6896
RIT:BBH:0864	0.4998	0.3332	0.6667	0.6068	0.3506	-0.3874
RIT:BBH:0866	0.4999	0.3332	0.6667	-0.6965	0.0029	-0.3948
RIT:BBH:0868	0.4999	0.3332	0.6667	0.2527	-0.2831	-0.7051
RIT:BBH:0869	0.5998	0.3749	0.6250	0.3757	0.5936	-0.3841
RIT:BBH:0871	0.5998	0.3749	0.6250	0.6007	0.3522	-0.3953
RIT:BBH:0872	0.4998	0.3332	0.6667	-0.2996	-0.2892	-0.6841
RIT:BBH:0873	0.5999	0.3749	0.6250	-0.2711	0.6421	-0.3936
RIT:BBH:0874	0.0667	0.0625	0.9367	0.5983	0.0331	0.6048
RIT:BBH:0875	0.5998	0.3749	0.6250	0.0572	0.6989	-0.3861
RIT:BBH:0877	0.4998	0.3332	0.6667	0.6094	0.3339	0.3980
RIT:BBH:0878	0.5998	0.3749	0.6250	-0.5745	0.3979	-0.3904
RIT:BBH:0879	0.4998	0.3332	0.6667	-0.5066	-0.4904	-0.3795

(Table continued)

TABLE VI. (*Continued*)

Run	q^r	m_1^r/m	m_2^r/m	χ_{1x}^r	χ_{1y}^r	χ_{1z}^r	χ_{2x}^r	χ_{2y}^r	χ_{2z}^r
RIT:BBH:0880	0.5998	0.3749	0.6250	-0.6959	0.0133	-0.3957
RIT:BBH:0881	0.4999	0.3332	0.6667	-0.6793	0.0161	0.4235
RIT:BBH:0883	0.4998	0.3332	0.6667	0.3887	0.5816	0.3895
RIT:BBH:0885	0.4999	0.3333	0.6667	-0.5613	0.3814	0.4247
RIT:BBH:0891	0.4999	0.3333	0.6667	0.0684	0.6929	0.3951
RIT:BBH:0892	0.4999	0.3333	0.6667	-0.2624	0.6303	0.4179
RIT:BBH:0894	0.4998	0.3332	0.6667	-0.5649	-0.5673	0.0129
RIT:BBH:0895	0.5999	0.3749	0.6250	-0.3049	0.7398	0.0181
RIT:BBH:0898	0.4999	0.3333	0.6667	0.5107	-0.6163	0.0045
RIT:BBH:0899	0.5998	0.3749	0.6250	0.7005	0.3877	0.0071
RIT:BBH:0900	0.4998	0.3332	0.6667	-0.2961	-0.2764	0.6908
RIT:BBH:0901	0.4999	0.3333	0.6667	0.4492	-0.5285	-0.3998
RIT:BBH:0902	0.5998	0.3749	0.6250	0.4380	0.6701	0.0053
RIT:BBH:0906	0.5999	0.3749	0.6250	0.0770	0.7967	0.0061
RIT:BBH:0907	0.4999	0.3332	0.6667	0.2436	-0.3190	0.6929
RIT:BBH:0915	0.5998	0.3749	0.6250	-0.3057	-0.2835	-0.6836
RIT:BBH:0916	0.4998	0.3332	0.6667	-0.4887	-0.4888	0.4042
RIT:BBH:0917	0.5999	0.3749	0.6250	-0.6526	0.4631	0.0178
RIT:BBH:0918	0.4999	0.3333	0.6667	0.4346	-0.5305	0.4129
RIT:BBH:0919	0.5998	0.3749	0.6250	-0.7992	0.0440	0.0151
RIT:BBH:0924	0.5998	0.3749	0.6250	0.2518	-0.3107	-0.6936
RIT:BBH:0925	1.0000	0.5000	0.5000	0.2397	0.0927	-0.4290
RIT:BBH:0927	0.5998	0.3749	0.6250	-0.5746	-0.5574	0.0142
RIT:BBH:0928	0.5998	0.3749	0.6250	-0.5161	-0.4788	-0.3814
RIT:BBH:0929	1.0000	0.5000	0.5000	0.1607	0.2031	-0.4278
RIT:BBH:0931	0.5999	0.3749	0.6250	0.4429	-0.5283	-0.4068
RIT:BBH:0932	1.0000	0.5000	0.5000	0.0575	0.2487	-0.4300
RIT:BBH:0933	1.0000	0.5000	0.5000	-0.0755	0.2395	-0.4324
RIT:BBH:0936	1.0000	0.5000	0.5000	-0.1831	0.1695	-0.4334
RIT:BBH:0939	0.5999	0.3749	0.6250	0.4855	-0.6363	0.0069
RIT:BBH:0940	1.0000	0.5000	0.5000	-0.2418	0.0401	-0.4359
RIT:BBH:0941	0.5998	0.3749	0.6250	-0.5158	-0.4647	0.3988
RIT:BBH:0944	1.0000	0.5000	0.5000	0.1333	-0.2167	-0.4305
RIT:BBH:0946	0.5999	0.3749	0.6250	0.4240	-0.5338	0.4195
RIT:BBH:0949	1.0000	0.4998	0.4998	0.5466	0.1804	-0.5567	0.5111	0.2160	0.5773
RIT:BBH:0950	1.0000	0.5000	0.5000	-0.2078	-0.1465	-0.4306
RIT:BBH:0951	1.0000	0.4998	0.4998	0.3865	0.4298	-0.5542	0.3628	0.4397	0.5623
RIT:BBH:0954	1.0000	0.4998	0.4998	0.1162	0.5685	-0.5517	0.1133	0.5564	0.5644
RIT:BBH:0955	1.0000	0.4998	0.4998	-0.1482	0.5543	-0.5584	-0.1483	0.5409	0.5713
RIT:BBH:0956	1.0000	0.5000	0.5000	0.4018	0.1684	-0.2455
RIT:BBH:0959	1.0000	0.4998	0.4998	-0.4272	0.3787	-0.5614	-0.4158	0.3745	0.5726
RIT:BBH:0966	1.0000	0.4998	0.4998	-0.4867	-0.3177	-0.5508	-0.4687	-0.3266	0.5610
RIT:BBH:0969	1.0000	0.4998	0.4998	-0.5651	0.1189	-0.5547	-0.5542	0.0978	0.5696
RIT:BBH:0970	1.0000	0.4998	0.4998	0.2869	-0.4894	-0.5650	0.2989	-0.4632	0.5806
RIT:BBH:0971	0.9662	0.4914	0.5086	-0.1845	0.7173	0.1472	-0.5296	0.2634	-0.0116
RIT:BBH:0972	1.0000	0.5000	0.5000	0.2766	0.3348	-0.2479
RIT:BBH:0975	0.9661	0.4913	0.5086	-0.4415	-0.5649	0.2373	0.0430	-0.5858	-0.0705
RIT:BBH:0977	0.9662	0.4914	0.5086	-0.2164	0.7089	0.1444	-0.5386	0.2448	-0.0038
RIT:BBH:0981	0.9661	0.4913	0.5086	0.4486	0.5930	0.1320	-0.0549	0.5886	0.0238
RIT:BBH:0982	1.0000	0.4998	0.4998	-0.0044	0.0041	0.8007	0.7631	0.2426	0.0075
RIT:BBH:0983	0.9661	0.4913	0.5086	0.5260	0.5250	0.1344	-0.0373	0.5903	-0.0129
RIT:BBH:0984	0.9661	0.4913	0.5086	0.5254	0.5216	0.1495	-0.0360	0.5905	0.0069
RIT:BBH:0985	1.0000	0.4998	0.4998	-0.0016	-0.0024	0.8007	0.5398	0.5914	0.0060
RIT:BBH:0986	1.0000	0.5000	0.5000	0.0720	0.4283	-0.2478
RIT:BBH:0989	0.9999	0.4998	0.4998	0.0043	-0.0120	0.8006	-0.2412	0.7633	0.0079

(Table continued)

TABLE VI. (*Continued*)

Run	q^r	m_1^r/m	m_2^r/m	χ_{1x}^r	χ_{1y}^r	χ_{1z}^r	χ_{2x}^r	χ_{2y}^r	χ_{2z}^r
RIT:BBH:0990	0.9999	0.4998	0.4998	0.0015	-0.0083	0.8007	0.1723	0.7818	0.0063
RIT:BBH:0995	0.9999	0.4998	0.4998	0.0059	-0.0125	0.8006	-0.5908	0.5402	0.0094
RIT:BBH:1010	1.0000	0.4998	0.4998	0.0059	-0.0096	0.8006	-0.7819	0.1722	0.0092
RIT:BBH:1013	1.0000	0.4998	0.4998	0.0031	-0.0009	0.8007	-0.6744	-0.4317	0.0066
RIT:BBH:1021	0.9945	0.4986	0.5014	-0.6964	0.2862	-0.5396	-0.5174	0.0099	0.6598
RIT:BBH:1026	0.9999	0.4998	0.4998	-0.0053	0.0127	0.8006	0.4307	-0.6748	0.0088
RIT:BBH:1053	0.2501	0.2000	0.7996	0.3987	0.0612	-0.6920
RIT:BBH:1055	0.2501	0.2000	0.7996	0.2387	0.3251	-0.6920
RIT:BBH:1056	0.2501	0.2000	0.7996	-0.3251	0.2388	-0.6920
RIT:BBH:1060	0.2501	0.2000	0.7996	0.1620	-0.3693	-0.6920
RIT:BBH:1061	0.2501	0.2000	0.7996	-0.0609	0.3987	-0.6920
RIT:BBH:1062	0.2501	0.2000	0.7996	-0.3693	-0.1622	-0.6920
RIT:BBH:1063	0.2501	0.2000	0.7996	-0.1010	0.7945	0.0048
RIT:BBH:1064	0.2501	0.2000	0.7996	0.7943	0.1031	0.0049
RIT:BBH:1065	0.2501	0.2000	0.7996	0.4896	0.6339	0.0042
RIT:BBH:1066	0.2501	0.2000	0.7996	-0.6338	0.4897	0.0055
RIT:BBH:1067	0.2501	0.2000	0.7996	-0.7408	-0.3047	0.0045
RIT:BBH:1068	0.2501	0.2000	0.7996	0.6891	0.0989	-0.3961
RIT:BBH:1069	0.2501	0.2000	0.7996	-0.6401	-0.2734	-0.3963
RIT:BBH:1070	0.2501	0.2000	0.7996	-0.5567	0.4181	-0.3959
RIT:BBH:1071	0.2501	0.2000	0.7996	0.4178	0.5567	-0.3964
RIT:BBH:1072	0.2501	0.2000	0.7996	0.2728	-0.6405	-0.3960
RIT:BBH:1073	0.2501	0.2000	0.7996	-0.0975	0.6892	-0.3962
RIT:BBH:1082	0.2501	0.2000	0.7996	0.3033	-0.7413	0.0051
RIT:BBH:1083	0.2501	0.2000	0.7996	0.6873	0.0798	0.4034
RIT:BBH:1084	0.2501	0.2000	0.7996	-0.6436	-0.2547	0.4030
RIT:BBH:1085	0.2501	0.2000	0.7996	-0.5414	0.4302	0.4041
RIT:BBH:1086	0.2501	0.2000	0.7996	0.4306	0.5421	0.4028
RIT:BBH:1087	0.2501	0.2000	0.7996	-0.0778	0.6875	0.4035
RIT:BBH:1917	0.2501	0.2000	0.7996	0.2531	-0.6437	0.4038
RIT:BBH:1918	0.2501	0.2000	0.7996	0.2516	0.3103	0.6942
RIT:BBH:1919	0.2501	0.2000	0.7996	0.1422	-0.3725	0.6947
RIT:BBH:1920	0.2501	0.2000	0.7996	-0.3096	0.2509	0.6948
RIT:BBH:1921	0.2501	0.2000	0.7996	-0.3727	-0.1433	0.6943
RIT:BBH:1922	0.2501	0.2000	0.7996	0.3968	0.0421	0.6945
RIT:BBH:1923	0.2501	0.2000	0.7996	-0.0409	0.3968	0.6945

simulations use as a reference starting gravitational wave frequency 30 Hz for a $50 M_\odot$ binary and is an additional set to those remaining 626 with reference frequency 10 Hz for a $50 M_\odot$ binary described in the Supplementary Material of Ref. [80].

In Tables V and VI, we provide the binary mass and spin parameters after they settle into a more physical value after radiating and absorbing the spurious gravitation wave content from the initial mathematical choice of conformal flatness. These relaxed values are calculated at a fiducial

$t = 200m$. Table V includes the new 134 quasicircular simulations (14 nonspinning) and the new 192 nonspinning eccentric started at 30 Hz gravitational wave frequency for a $50 M_\odot$ binary. Table VI adds the new 146 precessing quasicircular black hole binaries evolutions.

Finally, In Table VII, we give the values of the gravitational energy radiated during the simulation and the final black hole spin as measured through the (accurate) isolated horizon formalism [107] for all the new simulations reported in this paper.

TABLE VII. (*Continued*)

Run	$\delta\mathcal{M}^{IH}$	χ_{rem}^{IH}
RIT:eBBH:1253	0.046733 ± 0.000000	0.675896 ± 0.000025
RIT:eBBH:1254	0.046339 ± 0.000000	0.676326 ± 0.000033
RIT:eBBH:1255	0.046069 ± 0.000000	0.674826 ± 0.000024
RIT:eBBH:1256	0.046471 ± 0.000000	0.673351 ± 0.000034
RIT:eBBH:1257	0.047036 ± 0.000002	0.674493 ± 0.000009
RIT:eBBH:1258	0.046981 ± 0.000000	0.676785 ± 0.000032
RIT:eBBH:1259	0.046355 ± 0.000003	0.677713 ± 0.000008
RIT:eBBH:1260	0.045744 ± 0.000003	0.675969 ± 0.000019
RIT:eBBH:1261	0.045943 ± 0.000002	0.672745 ± 0.000009
RIT:eBBH:1262	0.046957 ± 0.000004	0.672155 ± 0.000017
RIT:eBBH:1263	0.047625 ± 0.000001	0.674976 ± 0.000015
RIT:eBBH:1264	0.047477 ± 0.000005	0.678288 ± 0.000014
RIT:eBBH:1265	0.046727 ± 0.000001	0.680254 ± 0.000017
RIT:eBBH:1266	0.045739 ± 0.000004	0.679837 ± 0.000020

(Table continued)

TABLE VII. (*Continued*)

Run	$\delta\mathcal{M}^{IH}$	χ_{rem}^{IH}
RIT:eBBH:1267	0.045000 ± 0.000001	0.676513 ± 0.000015
RIT:eBBH:1268	0.045296 ± 0.000001	0.671291 ± 0.000014
RIT:eBBH:1269	0.046854 ± 0.000000	0.668980 ± 0.000016
RIT:eBBH:1270	0.048370 ± 0.000000	0.671663 ± 0.000017
RIT:eBBH:1271	0.049083 ± 0.000001	0.676398 ± 0.000034
RIT:eBBH:1272	0.048671 ± 0.000001	0.685283 ± 0.000020
RIT:eBBH:1273	0.046070 ± 0.000001	0.693227 ± 0.000048
RIT:eBBH:1274	0.040769 ± 0.000001	0.694761 ± 0.000039
RIT:eBBH:1275	0.036018 ± 0.000000	0.686550 ± 0.000032
RIT:eBBH:1276	0.029100 ± 0.000000	0.651458 ± 0.000023
RIT:eBBH:1277	0.024914 ± 0.000001	0.598197 ± 0.000012
RIT:eBBH:1278	0.022543 ± 0.000001	0.528300 ± 0.000002
RIT:eBBH:1279	0.021366 ± 0.000001	0.438084 ± 0.000003
RIT:eBBH:1280	0.020991 ± 0.000001	0.313747 ± 0.000006
RIT:eBBH:1281	0.021129 ± 0.000001	0.100200 ± 0.000003

- [1] F. Pretorius, *Phys. Rev. Lett.* **95**, 121101 (2005).
- [2] M. Campanelli, C. O. Lousto, P. Marronetti, and Y. Zlochower, *Phys. Rev. Lett.* **96**, 111101 (2006).
- [3] J. G. Baker, J. Centrella, D.-I. Choi, M. Koppitz, and J. van Meter, *Phys. Rev. Lett.* **96**, 111102 (2006).
- [4] M. Campanelli, C. O. Lousto, H. Nakano, and Y. Zlochower, *Phys. Rev. D* **79**, 084010 (2009).
- [5] G. Lovelace, M. A. Scheel, R. Owen, M. Giesler, R. Katebi, B. Szilágyi, T. Chu, N. Demos, D. A. Hemberger, L. E. Kidder, H. P. Pfeiffer, and N. Afshari, *Classical Quantum Gravity* **32**, 065007 (2015).
- [6] Y. Zlochower, J. Healy, C. O. Lousto, and I. Ruchlin, *Phys. Rev. D* **96**, 044002 (2017).
- [7] C. O. Lousto and J. Healy, *Phys. Rev. Lett.* **125**, 191102 (2020).
- [8] C. O. Lousto and Y. Zlochower, *Phys. Rev. D* **88**, 024001 (2013).
- [9] C. O. Lousto, J. Healy, and H. Nakano, *Phys. Rev. D* **93**, 044031 (2016).
- [10] B. Szilagyi, J. Blackman, A. Buonanno, A. Taracchini, H. P. Pfeiffer, M. A. Scheel, T. Chu, L. E. Kidder, and Y. Pan, *Phys. Rev. Lett.* **115**, 031102 (2015).
- [11] M. Campanelli, C. O. Lousto, and Y. Zlochower, *Phys. Rev. D* **74**, 041501(R) (2006).
- [12] M. Hannam, S. Husa, B. Bruegmann, and A. Gopakumar, *Phys. Rev. D* **78**, 104007 (2008).
- [13] D. A. Hemberger, G. Lovelace, T. J. Loredo, L. E. Kidder, M. A. Scheel, B. Szilagyi, N. W. Taylor, and S. A. Teukolsky, *Phys. Rev. D* **88**, 064014 (2013).
- [14] J. Healy and C. O. Lousto, *Phys. Rev. D* **97**, 084002 (2018).
- [15] M. Campanelli, C. O. Lousto, Y. Zlochower, and D. Merritt, *Astrophys. J.* **659**, L5 (2007).
- [16] M. Campanelli, C. O. Lousto, Y. Zlochower, and D. Merritt, *Phys. Rev. Lett.* **98**, 231102 (2007).
- [17] F. Herrmann, I. Hinder, D. M. Shoemaker, P. Laguna, and R. A. Matzner, *Phys. Rev. D* **76**, 084032 (2007).
- [18] D. Pollney, C. Reisswig, L. Rezzolla, B. Szilágyi, M. Ansorg, B. Deris, P. Diener, E. N. Dorband, M. Koppitz, A. Nagar, and E. Schnetter, *Phys. Rev. D* **76**, 124002 (2007).
- [19] J. G. Baker, J. Centrella, D.-I. Choi, M. Koppitz, J. R. van Meter, and M. C. Miller, *Astrophys. J.* **653**, L93 (2006).
- [20] J. A. González, M. D. Hannam, U. Sperhake, B. Brugmann, and S. Husa, *Phys. Rev. Lett.* **98**, 231101 (2007).
- [21] J. D. Schnittman, A. Buonanno, J. R. van Meter, J. G. Baker, W. D. Boggs, J. Centrella, B. J. Kelly, and S. T. McWilliams, *Phys. Rev. D* **77**, 044031 (2008).
- [22] C. O. Lousto and Y. Zlochower, *Phys. Rev. Lett.* **107**, 231102 (2011).
- [23] C. O. Lousto and J. Healy, *Phys. Rev. Lett.* **114**, 141101 (2015).
- [24] C. O. Lousto and J. Healy, *Phys. Rev. D* **93**, 124074 (2016).
- [25] C. O. Lousto and J. Healy, *Phys. Rev. D* **99**, 064023 (2019).
- [26] P. Schmidt, M. Hannam, S. Husa, and P. Ajith, *Phys. Rev. D* **84**, 024046 (2011).
- [27] C. O. Lousto and Y. Zlochower, *Phys. Rev. D* **89**, 021501 (2014).
- [28] L. Pekowsky, R. O’Shaughnessy, J. Healy, and D. Shoemaker, *Phys. Rev. D* **88**, 024040 (2013).
- [29] S. Ossokine, M. Boyle, L. E. Kidder, H. P. Pfeiffer, M. A. Scheel, and B. Szilagyi, *Phys. Rev. D* **92**, 104028 (2015).
- [30] J. Blackman, S. E. Field, M. A. Scheel, C. R. Galley, D. A. Hemberger, P. Schmidt, and R. Smith, *Phys. Rev. D* **95**, 104023 (2017).

- [31] J. Blackman, S. E. Field, M. A. Scheel, C. R. Galley, C. D. Ott, M. Boyle, L. E. Kidder, H. P. Pfeiffer, and B. Szilgyi, *Phys. Rev. D* **96**, 024058 (2017).
- [32] V. Varma, S. E. Field, M. A. Scheel, J. Blackman, L. E. Kidder, and H. P. Pfeiffer, *Phys. Rev. D* **99**, 064045 (2019).
- [33] B. P. Abbott *et al.* (Virgo, LIGO Scientific Collaborations), *Phys. Rev. Lett.* **116**, 241102 (2016).
- [34] B. Abbott *et al.* (Virgo, LIGO Scientific Collaborations), *Phys. Rev. Lett.* **116**, 061102 (2016).
- [35] B. P. Abbott *et al.* (Virgo, LIGO Scientific Collaborations), *Phys. Rev. Lett.* **116**, 241103 (2016).
- [36] B. P. Abbott *et al.* (Virgo, LIGO Scientific Collaborations), *Phys. Rev. X* **6**, 041015 (2016).
- [37] B. P. Abbott *et al.* (Virgo, LIGO Scientific Collaborations), *Classical Quantum Gravity* **34**, 104002 (2017).
- [38] B. P. Abbott *et al.* (Virgo, LIGO Scientific Collaborations), *Phys. Rev. D* **94**, 064035 (2016).
- [39] B. P. Abbott *et al.* (Virgo, LIGO Scientific Collaborations), *Phys. Rev. D* **93**, 122004 (2016); **94**, 069903(E) (2016).
- [40] G. Lovelace *et al.*, *Classical Quantum Gravity* **33**, 244002 (2016).
- [41] J. Healy *et al.*, *Phys. Rev. D* **97**, 064027 (2018).
- [42] A. H. Mroue, M. A. Scheel, B. Szilagyi, H. P. Pfeiffer, M. Boyle *et al.*, *Phys. Rev. Lett.* **111**, 241104 (2013).
- [43] J. Blackman, S. E. Field, C. R. Galley, B. Szilagyi, M. A. Scheel, M. Tiglio, and D. A. Hemberger, *Phys. Rev. Lett.* **115**, 121102 (2015).
- [44] T. Chu, H. Fong, P. Kumar, H. P. Pfeiffer, M. Boyle, D. A. Hemberger, L. E. Kidder, M. A. Scheel, and B. Szilagyi, *Classical Quantum Gravity* **33**, 165001 (2016).
- [45] M. Boyle *et al.*, *Classical Quantum Gravity* **36**, 195006 (2019).
- [46] K. Jani, J. Healy, J. A. Clark, L. London, P. Laguna, and D. Shoemaker, *Classical Quantum Gravity* **33**, 204001 (2016).
- [47] J. Healy, C. O. Lousto, Y. Zlochower, and M. Campanelli, *Classical Quantum Gravity* **34**, 224001 (2017).
- [48] J. Healy, C. O. Lousto, J. Lange, R. O’Shaughnessy, Y. Zlochower, and M. Campanelli, *Phys. Rev. D* **100**, 024021 (2019).
- [49] J. Healy and C. O. Lousto, *Phys. Rev. D* **102**, 104018 (2020).
- [50] J. Healy, C. O. Lousto, J. Lange, and R. O’Shaughnessy, *Phys. Rev. D* **102**, 124053 (2020).
- [51] E. A. Tassone, P. A. Mandrilli, C. N. Kozameh, G. D. Quiroga, and J. I. Nieva, *Phys. Rev. D* **104**, 084038 (2021).
- [52] <https://ccrgpages.rit.edu/~RITCatalog/>.
- [53] Y. Zlochower, J. G. Baker, M. Campanelli, and C. O. Lousto, *Phys. Rev. D* **72**, 024021 (2005).
- [54] T. Nakamura, K. Oohara, and Y. Kojima, *Prog. Theor. Phys. Suppl.* **90**, 1 (1987).
- [55] M. Shibata and T. Nakamura, *Phys. Rev. D* **52**, 5428 (1995).
- [56] T. W. Baumgarte and S. L. Shapiro, *Phys. Rev. D* **59**, 024007 (1998).
- [57] D. Alic, C. Bona-Casas, C. Bona, L. Rezzolla, and C. Palenzuela, *Phys. Rev. D* **85**, 064040 (2012).
- [58] C. O. Lousto and Y. Zlochower, *Phys. Rev. D* **77**, 024034 (2008).
- [59] Y. Zlochower, M. Ponce, and C. O. Lousto, *Phys. Rev. D* **86**, 104056 (2012).
- [60] J. Healy and C. O. Lousto, *Phys. Rev. D* **95**, 024037 (2017).
- [61] Cactus Computational Toolkit home page: <http://cactuscode.org>.
- [62] E. Schnetter, S. H. Hawley, and I. Hawke, *Classical Quantum Gravity* **21**, 1465 (2004).
- [63] F. Löffler, J. Faber, E. Bentivegna, T. Bode, P. Diener, R. Haas, I. Hinder, B. C. Mundim, C. D. Ott, E. Schnetter, G. Allen, M. Campanelli, and P. Laguna, *Classical Quantum Gravity* **29**, 115001 (2012).
- [64] Einstein Toolkit home page: <http://einstein toolkit.org>.
- [65] J. Thornburg, *Classical Quantum Gravity* **21**, 743 (2004).
- [66] M. Campanelli, C. O. Lousto, Y. Zlochower, B. Krishnan, and D. Merritt, *Phys. Rev. D* **75**, 064030 (2007).
- [67] M. Ansorg, B. Brügmann, and W. Tichy, *Phys. Rev. D* **70**, 064011 (2004).
- [68] J. Healy, C. O. Lousto, H. Nakano, and Y. Zlochower, *Classical Quantum Gravity* **34**, 145011 (2017).
- [69] I. Ruchlin, J. Healy, C. O. Lousto, and Y. Zlochower, *Phys. Rev. D* **95**, 024033 (2017).
- [70] J. Healy, I. Ruchlin, C. O. Lousto, and Y. Zlochower, *Phys. Rev. D* **94**, 104020 (2016).
- [71] M. Campanelli and C. O. Lousto, *Phys. Rev. D* **59**, 124022 (1999).
- [72] C. O. Lousto and Y. Zlochower, *Phys. Rev. D* **76**, 041502 (R) (2007).
- [73] H. Nakano, J. Healy, C. O. Lousto, and Y. Zlochower, *Phys. Rev. D* **91**, 104022 (2015).
- [74] M. Boyle, *Phys. Rev. D* **93**, 084031 (2016).
- [75] B. J. Kelly and J. G. Baker, *Phys. Rev. D* **87**, 084004 (2013).
- [76] J. Healy, C. O. Lousto, and Y. Zlochower, *Phys. Rev. D* **90**, 104004 (2014).
- [77] J. Healy, C. O. Lousto, and Y. Zlochower, *Phys. Rev. D* **96**, 024031 (2017).
- [78] J. Healy *et al.*, *Phys. Rev. D* **97**, 064027 (2018).
- [79] DataTables home page: <https://datatables.net>.
- [80] V. Gayathri, J. Healy, J. Lange, B. O’Brien, M. Szczerpanczyk, I. Bartos, M. Campanelli, S. Klimenko, C. O. Lousto, and R. O’Shaughnessy, *Nat. Astron.* **6**, 344 (2022).
- [81] D. Keitel *et al.*, *Phys. Rev. D* **96**, 024006 (2017).
- [82] V. Varma, D. Gerosa, L. C. Stein, F. Hébert, and H. Zhang, *Phys. Rev. Lett.* **122**, 011101 (2019).
- [83] V. Varma, S. E. Field, M. A. Scheel, J. Blackman, D. Gerosa, L. C. Stein, L. E. Kidder, and H. P. Pfeiffer, *Phys. Rev. Research* **1**, 033015 (2019).
- [84] J. D. Schnittman and J. H. Krolik, *Astrophys. J.* **806**, 88 (2015).
- [85] C. Nixon, *Mon. Not. R. Astron. Soc.* **423**, 2597 (2012).
- [86] F. Antonini and H. B. Perets, *Astrophys. J.* **757**, 27 (2012).
- [87] J. Samsing, M. MacLeod, and E. Ramirez-Ruiz, *Astrophys. J.* **784**, 71 (2014).
- [88] J. Shapiro Key and N. J. Cornish, *Phys. Rev. D* **83**, 083001 (2011).
- [89] D. J. D’Orazio and J. Samsing, *Mon. Not. R. Astron. Soc.* **481**, 4775 (2018).

- [90] B.-M. Hoang, S. Naoz, B. Kocsis, W. Farr, and J. McIver, *Astrophys. J.* **875**, L31 (2019).
- [91] A. Sesana, *Phys. Rev. Lett.* **116**, 231102 (2016).
- [92] S. Vitale, *Phys. Rev. Lett.* **117**, 051102 (2016).
- [93] E. Barausse, N. Yunes, and K. Chamberlain, *Phys. Rev. Lett.* **116**, 241104 (2016).
- [94] N. Rosato, J. Healy, and C. O. Lousto, *Phys. Rev. D* **103**, 104068 (2021).
- [95] A. Nagar, J. Healy, C. O. Lousto, S. Bernuzzi, and A. Albertini, [arXiv:2202.05643](https://arxiv.org/abs/2202.05643).
- [96] S. Brandt and B. Brügmann, *Phys. Rev. Lett.* **78**, 3606 (1997).
- [97] B. P. Abbott *et al.* (LIGO Scientific, Virgo Collaborations), *Phys. Rev. X* **9**, 031040 (2019).
- [98] J. Sadiq, Y. Zlochower, R. O’Shaughnessy, and J. Lange, *Phys. Rev. D* **102**, 024012 (2020).
- [99] E. Barausse, V. Morozova, and L. Rezzolla, *Astrophys. J.* **758**, 63 (2012).
- [100] L. Rezzolla, E. Barausse, E. N. Dorband, D. Pollney, C. Reisswig, J. Seiler, and S. Husa, *Phys. Rev. D* **78**, 044002 (2008).
- [101] F. Hofmann, E. Barausse, and L. Rezzolla, *Astrophys. J.* **825**, L19 (2016).
- [102] X. Jiménez-Forteza, D. Keitel, S. Husa, M. Hannam, S. Khan, and M. Pürrer, *Phys. Rev. D* **95**, 064024 (2017).
- [103] C. O. Lousto, M. Campanelli, Y. Zlochower, and H. Nakano, *Classical Quantum Gravity* **27**, 114006 (2010).
- [104] C. O. Lousto and Y. Zlochower, *Phys. Rev. D* **89**, 104052 (2014).
- [105] Y. Zlochower and C. O. Lousto, *Phys. Rev. D* **92**, 024022 (2015).
- [106] D. Gerosa, F. Hébert, and L. C. Stein, *Phys. Rev. D* **97**, 104049 (2018).
- [107] O. Dreyer, B. Krishnan, D. Shoemaker, and E. Schnetter, *Phys. Rev. D* **67**, 024018 (2003).